

The computational simulation of the reflection spectra of copper red glaze

Cite as: AIP Advances 12, 095319 (2022); <https://doi.org/10.1063/5.0095570>

Submitted: 18 April 2022 • Accepted: 29 August 2022 • Published Online: 26 September 2022

 Gen Li and  Yong Lei



View Online



Export Citation



CrossMark



The computational simulation of the reflection spectra of copper red glaze

Cite as: AIP Advances 12, 095319 (2022); doi: 10.1063/5.0095570

Submitted: 18 April 2022 • Accepted: 29 August 2022 •

Published Online: 26 September 2022



View Online



Export Citation



CrossMark

Gen Li and Yong Lei^a

AFFILIATIONS

Department of Conservation Science and Technology, The Palace Museum, Beijing 100009, People's Republic of China

^a**Permanent address:** Palace Museum, Beijing 100009, People's Republic of China. **Author to whom correspondence should be addressed:** leiyong@dpm.org.cn. **Tel.:** +86 010-85007260

ABSTRACT

Owing to the limitation of traditional analytical methods, the coloration mechanism of copper red glaze has been disputed in the academic field for a long time, which mainly focuses on whether the color agent is metallic copper nanoparticles or cuprous oxide (Cu_2O) nanoparticles. Based on Mie scattering theory, this work calculated the reflection spectra of nanoparticles uniformly dispersed in transparent glaze with different types, diameters, and volume fractions, then discussed the differences between the reflection spectra of metallic copper and cuprous oxide as scatterers, calculated the corresponding $L^*a^*b^*$ values, and compared them with the experimental results. This work provides a feasible and convenient method to distinguish these two coloration mechanisms.

© 2022 Author(s). All article content, except where otherwise noted, is licensed under a Creative Commons Attribution (CC BY) license (<http://creativecommons.org/licenses/by/4.0/>). <https://doi.org/10.1063/5.0095570>

I. INTRODUCTION

As a famous kind of porcelain in ancient China, copper red glaze has always been famous for its beautiful appearance and high firing difficulty and also received much attention from the academic community. Generally speaking, the copper red glaze was first produced in Changsha Kiln in Tang Dynasty, but at that time the red glaze was mainly used as local decoration because the kilnmen did not have the technique to control the formation of copper red glaze perfectly. After the development of several hundred years, genuine copper-red glaze was thought to emerge in the late Yuan Dynasty and reach its peak in the early Ming Dynasty, especially during the reign of Yongle and Xuande, and some famous types of products were invented, such as bright red and sacrificial red glaze. When it comes to the Qing Dynasty, the techniques of firing perfect copper red glaze were lost so the kilnmen invented new recipes to imitate the artifacts of the Ming Dynasty and produce several new types of copper red glaze, such as peach bloom glaze and Lang Kiln red glaze. Figure 1 shows two typical copper red glaze artifacts of ancient China, namely the monk hat pot with bright red glaze produced in the Ming Dynasty, and the plum vase with sacrificial red glaze produced in the Qing Dynasty.

The current research on copper red glaze mainly focuses on its firing process, raw material source, coloration mechanism, and so on. In the study of the coloration mechanism, the consensus of the academic community is that the red color comes from copper-containing nanoparticles in the glaze but not copper ions because Cu^+ ion is almost colorless, and Cu^{2+} ion generally appears green. On the other hand, these particles may be metallic copper or cuprous oxide (Cu_2O) because both of them are red in their bulk states, but it is still under debate which one dominates. Nowadays, more scholars tend to think that the colorant in the copper red glaze is mainly metallic copper nanoparticles,^{1–3} but scholars, who think cuprous oxide nanoparticles are the main colorant, also give some evidence.^{4,5} In addition, for ancient ceramics with complex hues, such as Jun kiln porcelain, some scholars also analyze it in combination with the microstructure inside the glaze layer, such as liquid–liquid phase separation to form small droplets of the second phase and regard its hue as the joint action of nanostructures and metal ions.⁶

Generally speaking, the analysis methods of copper red glaze can be summarized as follows: XRD is used to analyze the phases,^{1,7} XRF and x-ray energy dispersive spectrum (EDS) are used to analyze the type and content of elements,^{1,7,8} XPS^{9,10} and x-ray absorption



FIG. 1. (a) Monk hat pot with bright red glaze produced during the Xuande reign period, Ming Dynasty and (b) Plum vase with sacrificial red glaze produced during the Yongzheng reign period, Qing Dynasty (courtesy of the Palace Museum).

nearedge structure (XANES)^{11–15} are used to analyze the valence state, and then at the micro level, SEM and TEM are used to observe the sizes and phases of particles,^{1,3,6} while EXAFS is used to study the coordination relationship of atoms.^{2,16} These methods have greatly promoted people's understanding of copper red glaze, but they are still insufficient to solve the problem of the coloration mechanism.

For example, the spatial resolution of conventional chemical analytical methods, such as XPS and XRF, is confined to micrometers, which makes the signal collected come from not only nanoparticles but also the transparent glaze. In fact, according to the previous reference, Cu⁺ ion also exists in a transparent glaze, and for a typical sacrificial red glaze, the content of copper in the colorless layer is even higher than that in the red layer.¹² From this point of view, even if XPS or XRF gives the signal of Cu⁰ in the red layer, we cannot assert how many percent of nanoparticles are metallic copper nanoparticles. Electron microscopy can accurately determine the size and phase structures of nanoparticles; however, the number of observed particles is small, and the statistics is not strong enough. In addition, these methods above are all invasive because the cross-section sample is needed in the study of copper red glaze.

The reflection spectrum is indeed a genuine non-invasive method. However, if we want to use the reflection spectrum as an indicator of metallic copper or cuprous oxide nanoparticles, two standard samples with pure metallic copper/cuprous oxide nanoparticles uniformly dispersed are necessary to use their reflection spectra as references, but producing such a glaze sample with homogeneously dispersed Cu₂O nanoparticles is difficult. To sum up, it is not so easy to quickly determine whether a given copper red glaze sample, especially an unbroken artifact, is colored by metallic copper particles or cuprous oxide particles.

When the experimental methods meet the bottleneck, the theoretical computational simulation often gives us new inspiration. Previously, Pradell *et al.* calculated the absorption and scattering cross sections of nanoparticles based on Mie scattering theory

and, on that basis, discussed the optical properties of the system.¹⁷ Cuvelier *et al.* used the four-flux model to discuss the influence of copper particles with different radii and different volume fractions on coloration and also calculated the scattering behavior of the system when cuprous oxide was coated on the surface of metallic copper particles.¹⁸ This paper will start from the Mie scattering theory to establish a numerical calculation framework based on multiple scattering and simulate the reflection spectrum of transparent glaze with uniformly dispersed nanoparticles of different sizes, different volume fractions, and different materials. Then, the authors will discuss the difference in reflection spectrum between systems with metallic copper and cuprous oxide particles as colorants and provide a new perspective on the coloration of copper red glaze.

II. COMPUTATIONAL METHOD

A. Basic theory of Mie scattering

The Mie scattering theory of spherical scatterers will be briefly introduced in this section, which is mainly summarized by Bohren and Huffman¹⁹ and the manuscript of Mätzler.²⁰

1. Expansion of the incident and scattered waves

Consider the incoming monochromatic plane wave on the surface of a sphere,

$$\mathbf{E}_i = E_0 e^{i\mathbf{k} \cdot \mathbf{r} \cos \theta} \hat{\mathbf{e}}_x$$

In the inner and outside parts of this sphere, the electromagnetic field should satisfy the Maxwell equations. Using a spherical coordinate system, the incoming plane wave can be written as the summation of a series of spherical harmonic functions,

$$\mathbf{E}_i = E_0 \sum_{n=1}^{\infty} i^n \frac{2n+1}{n(n+1)} \left(\mathbf{M}_{oln}^{(1)} - i \mathbf{N}_{eln}^{(1)} \right).$$

The inner and scattered electromagnetic fields of the sphere can be written in the following form:

$$\begin{aligned} \mathbf{E}_l &= \sum_{n=1}^{\infty} E_n \left(c_n \mathbf{M}_{oln}^{(1)} - id_n \mathbf{N}_{eln}^{(1)} \right), \\ \mathbf{H}_l &= \frac{-\mathbf{k}_l}{\omega \mu_l} \sum_{n=1}^{\infty} E_n \left(d_n \mathbf{M}_{eln}^{(1)} + ic_n \mathbf{N}_{oln}^{(1)} \right), \\ \mathbf{E}_s &= \sum_{n=1}^{\infty} E_n \left(ia_n \mathbf{N}_{eln}^{(3)} - b_n \mathbf{M}_{oln}^{(3)} \right), \\ \mathbf{H}_s &= \frac{\mathbf{k}}{\omega \mu} \sum_{n=1}^{\infty} E_n \left(ib_n \mathbf{N}_{oln}^{(3)} + a_n \mathbf{M}_{eln}^{(3)} \right), \end{aligned}$$

where

$$\begin{aligned} \mathbf{M}_{oln} &= \cos \phi \pi_n(\cos \theta) z_n(\rho) \hat{\mathbf{e}}_\theta - \sin \phi \pi_n(\cos \theta) z_n(\rho) \hat{\mathbf{e}}_\phi, \\ \mathbf{M}_{eln} &= -\sin \phi \pi_n(\cos \theta) z_n(\rho) \hat{\mathbf{e}}_\theta - \cos \phi \pi_n(\cos \theta) z_n(\rho) \hat{\mathbf{e}}_\phi, \\ \mathbf{N}_{oln} &= \sin \phi n(n+1) \sin \theta \pi_n(\cos \theta) \frac{z_n(\rho)}{\rho} \hat{\mathbf{e}}_r \\ &\quad + \sin \phi \tau_n(\cos \theta) \frac{[\rho z_n(\rho)]'}{\rho} \hat{\mathbf{e}}_\theta + \cos \phi \pi_n(\cos \theta) \frac{[\rho z_n(\rho)]'}{\rho} \hat{\mathbf{e}}_\phi, \\ \mathbf{N}_{eln} &= \cos \phi n(n+1) \sin \theta \pi_n(\cos \theta) \frac{z_n(\rho)}{\rho} \hat{\mathbf{e}}_r \\ &\quad + \cos \phi \tau_n(\cos \theta) \frac{[\rho z_n(\rho)]'}{\rho} \hat{\mathbf{e}}_\theta - \sin \phi \pi_n(\cos \theta) \frac{[\rho z_n(\rho)]'}{\rho} \hat{\mathbf{e}}_\phi, \end{aligned}$$

and we have

$$\pi_n = \frac{P_n^1}{\sin \theta}, \quad \tau_n = \frac{dP_n^1}{d\theta}.$$

For the inner magnetic field, z_n stands for spherical Bessel function $j_n(k_1 r)$; and for the scattered magnetic field, it stands for spherical Bessel function $h_n^{(1)}(kr)$,

$$\begin{aligned} j_n(\rho) &= \sqrt{\frac{\pi}{2\rho}} J_{n+1/2}(\rho), \quad y_n(\rho) = \sqrt{\frac{\pi}{2\rho}} Y_{n+1/2}(\rho), \\ h_n^{(1)}(\rho) &= j_n(\rho) + iy_n(\rho), \quad h_n^{(2)}(\rho) = j_n(\rho) - iy_n(\rho), \end{aligned}$$

and the four series of scattering parameters can be written as

$$\begin{aligned} a_n &= \frac{m^2 j_n(mx)[xj_n(x)]' - j_n(x)[mxj_n(mx)]'}{m^2 j_n(mx)[xh_n^{(1)}(x)]' - h_n^{(1)}(x)[mxj_n(mx)]'}, \\ b_n &= \frac{j_n(mx)[xj_n(x)]' - j_n(x)[mxj_n(mx)]'}{j_n(mx)[xh_n^{(1)}(x)]' - h_n^{(1)}(x)[mxj_n(mx)]'}, \\ c_n &= \frac{j_n(x)[xh_n^{(1)}(x)]' - h_n^{(1)}(x)[xj_n(x)]'}{j_n(mx)[xh_n^{(1)}(x)]' - h_n^{(1)}(x)[mxj_n(mx)]'}, \\ d_n &= \frac{mj_n(x)[xh_n^{(1)}(x)]' - mh_n^{(1)}(x)[xj_n(x)]'}{m^2 j_n(mx)[xh_n^{(1)}(x)]' - h_n^{(1)}(x)[mxj_n(mx)]'}. \end{aligned}$$

In fact, the former two series of scattering parameters, namely a_n and b_n , are essential for the calculation of scattering and extinction cross section.

In addition, m is the refraction index of the sphere scatterer relative to the surrounding medium. Generally speaking, the refraction index of an arbitrary medium is a complex number $n + ik$. The real part n is equal to the ratio between vacuum light speed and the phase velocity of light in the medium, and the imaginary part k stands for the absorption of light. Furthermore, the refractive index of the same medium to different wavelengths of light is also different, which is called the dispersion of the medium. n and k are usually called the optical constants of matter.

2. Several important parameters

Define $\sigma_{\text{abs}}(\lambda, d)$, $\sigma_{\text{sca}}(\lambda, d)$, and $\sigma_{\text{ext}}(\lambda, d) = \sigma_{\text{abs}}(\lambda, d) + \sigma_{\text{sca}}(\lambda, d)$ to be the absorption, scattering, and extinction cross section, respectively, of a copper-containing particle with diameter d relative to the light of wavelength λ , and they are the functions of λ and d . Theoretical scattering and extinction cross section can be given based on the results above,²⁰

$$\begin{aligned} C_{\text{sca}} &= \frac{W_s}{I_i} = \frac{2\pi}{k^2} \sum_{n=1}^{\infty} (2n+1)(|a_n|^2 + |b_n|^2), \\ C_{\text{ext}} &= \frac{W_{\text{ext}}}{I_i} = \frac{2\pi}{k^2} \sum_{n=1}^{\infty} (2n+1)\text{Re}(a_n + b_n), \end{aligned}$$

and the difference between extinction and scattering cross sections is the absorption cross section.

These cross sections can be written as the product between corresponding dimensionless coefficients and the projection areas of these particles, namely $\sigma_{\text{abs}}(\lambda, d) = Q_{\text{abs}}(\lambda, d) \times \pi d^2/4$, $\sigma_{\text{sca}}(\lambda, d) = Q_{\text{sca}}(\lambda, d) \times \pi d^2/4$, and $Q_{\text{ext}}(\lambda, d) = Q_{\text{abs}}(\lambda, d) + Q_{\text{sca}}(\lambda, d)$. If we define $x = ka$, where k is the wave vector, and a is the radius of the spherical particle, then the corresponding dimensionless scattering and extinction coefficients can be defined as

$$\begin{aligned} Q_{\text{sca}} &= \frac{2}{x^2} \sum_{n=1}^{\infty} (2n+1)(|a_n|^2 + |b_n|^2), \\ Q_{\text{ext}} &= \frac{2}{x^2} \sum_{n=1}^{\infty} (2n+1)\text{Re}(a_n + b_n). \end{aligned}$$

In this work, these three dimensionless coefficients can be calculated by MATLAB based on Mie scattering theory for any given wavelength and particle diameter.²⁰

B. Basic assumptions

In order to highlight the main research object and simplify the calculations, some assumptions are made first:

- (1) The reflection rate of the upper glaze surface is a constant r_1 ($0 \leq r_1 \leq 1$) for all the wavelengths.
- (2) The reflection rate of the ceramic body is a constant r_2 ($0 \leq r_2 \leq 1$) for all the wavelengths.
- (3) The copper-containing particles are uniformly dispersed in each transparent glaze layer paralleled to the glaze surface.
- (4) The absorption character of pure transparent glaze satisfies the Lambert–Bill law. Assume that the light intensity decreases to be $s_0 < 1$ after passing the whole transparent glaze layer. If the transparent glaze layer is uniformly divided into N thin layers, then the light intensity will reduce to $s = \sqrt[N]{s_0}$ after passing each thin layer.
- (5) The incident light is perpendicular to the glaze, and the scattering light is simplified as forward scattering and backward scattering terms.
- (6) All the copper-containing particles are spheres.

In the following, we will discuss the calculation details based on the assumptions above.

C. Interaction between uniformly distributed copper-containing particles and light

Copper-containing particles will absorb and scatter the incident light of any wavelength λ . Generally, the light can be scattered in any direction, but for simplicity in our system, the scattering light is simplified as forward scattering and backward scattering, and the forward/backward ratio is defined as the ratio of the power of forward and backward light scattering by a spherical particle.

Here, the “forward” means that the angle between scattered light and incident light lies at $0\text{--}90^\circ$, and the “backward” means that the angle between scattered light and incident light lies at $90\text{--}180^\circ$. The forward/backward ratio R_b can be calculated by integrating the power of scattered light under different scattering angles.

Define the volume fraction of copper-containing particles in the glaze as ω , then the particle number in per unit volume (namely, the number density) is

$$\rho = 6\omega/\pi d^3.$$

Under the assumption that the particles are uniformly dispersed, we can divide the glaze layer into N thin layers along the

depth direction and define t as the thickness of each layer. If the intensity of incident light is I_0 , the absorbed intensity I_{abs} , forward scattered intensity I_{scaf} , and backward scattered intensity I_{sca} are

$$\begin{cases} I_{\text{abs}} = I_0[1 - \exp(-n\sigma_{\text{abs}}t)] = I_0[1 - \exp(-tC_a(\lambda, d))], \\ I_{\text{scaf}} = I_{\text{sca}} \frac{r}{1+r} = \frac{rI_0}{1+r}[1 - \exp(-tC_s(\lambda, d))], \\ I_{\text{sca}} = I_{\text{sca}} \frac{1}{1+r} = \frac{I_0}{1+r}[1 - \exp(-tC_s(\lambda, d))], \end{cases}$$

where $C_a(\lambda, d)$ and $C_s(\lambda, d)$ are the product of corresponding absorption and scattering cross section and the particle number density, and they stand for the absorption and scattering intensity of the glaze with unit thickness.

Then, the light intensity I_f along the original direction and light intensity I_b along the backward direction are

$$\begin{cases} I_f = (I_0 - I_{\text{abs}} - I_{\text{sca}})s + I_{\text{scaf}} = C_{\text{ff}}(\lambda, d, t)I_0, \\ I_b = I_{\text{sca}} = C_{\text{bb}}(\lambda, d, t)I_0, \end{cases}$$

where

$$\begin{cases} C_{\text{ff}}(\lambda, d, t) = s[\exp(-tC_a(\lambda, d)) + \exp(-tC_s(\lambda, d)) - 1] + \frac{r[1 - \exp(-tC_s(\lambda, d))]}{1+r}, \\ C_{\text{bb}}(\lambda, d, t) = \frac{[1 - \exp(-tC_s(\lambda, d))]}{r+1}. \end{cases}$$

Now we will analyze the mathematical relationship of the light intensities in different thin layers. As shown in Fig. 2(a), if we number the uppermost glaze thin layer as 1 and the glaze thin layer contact with the body as N , then we can formally number the air as layer 0, and the ceramic body as layer $N+1$.

For the thin layer numbered as i , if we define I_i as the intensity of the incident light into the upper surface, O_i as the intensity of the outgoing light away from the upper surface, as shown in Fig. 2(b),

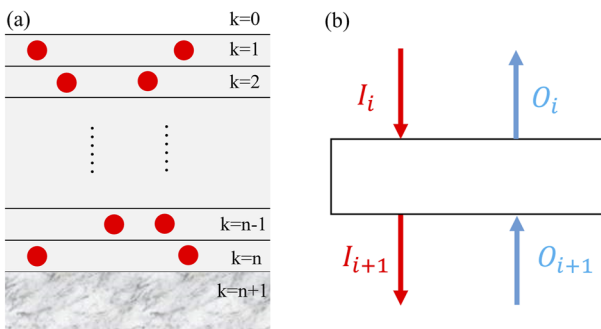


FIG. 2. Schematic diagram of the system with uniformly distributed copper-containing particles. (a) The transparent glaze is divided into N thin layers, and the air and body can be formally regarded as layer 0 and layer $N+1$, respectively. (b) Incident and outgoing light from the upper and lower surfaces of the thin layer i .

then the outgoing light O_{i+1} away from the upper surface of thin layer $i+1$ will be the incident light into the lower surface of thin layer i , and the incident light I_{i+1} into the upper surface of thin layer $i+1$ is also the outgoing light away from the lower surface of thin layer i .

Based on these relationships, the outgoing light intensity away from the thin layer i can be written as

$$O_i = C_{\text{bb}}(\lambda, d)I_i + C_{\text{ff}}(\lambda, d, t)O_{i+1}.$$

Similarly, the outgoing light intensity away from the lower surface of the thin layer i can be written as

$$I_{i+1} = C_{\text{ff}}(\lambda, d, t)I_i + C_{\text{bb}}(\lambda, d)O_{i+1}.$$

The above two formulas are the relationships that the light should obey in the glaze, and the boundary conditions are also needed to determine the light intensity at any depth in the glaze.

First, at the body–glaze interface, according to assumption (2), we have $O_{N+1} = r_2 I_{N+1}$.

Second, assume the intensity of incident light into the upper surface to be 1, namely $I_0 = 1$. Taking the refraction and reflection at the glaze–air boundary into consideration, we have $O_0 = r_1 I_0 + (1 - r_1)O_1$ and $I_1 = (1 - r_1)I_0 + r_1 O_1$.

Solving the question above is equivalent to solving a system of linear equations with $2N + 4$ components. Denote $I_k = x_{2k+1}$ and

$O_k = x_{2k+2}$ (where $k = 0, 1, 2, \dots, N, N + 1$), then the six formulas above can be rewritten as

$$\begin{cases} x_1 = 1, \\ r_1 x_1 - x_2 + (1 - r_1) x_4 = 0, \\ (1 - r_1) x_1 - x_3 + r_1 x_4 = 0, \\ C_{bb}(\lambda, d, t) x_{2k+1} - x_{2k+2} + C_{ff}(\lambda, d, t) x_{2k+4} = 0 \quad (k > 0), \\ C_{ff}(\lambda, d, t) x_{2k+1} - x_{2k+3} + C_{bb}(\lambda, d, t) x_{2k+4} = 0 \quad (k > 0), \\ r_2 x_{2N+3} - x_{2N+4} = 0. \end{cases}$$

The solved x_2 is the outgoing light intensity away from the glaze surface to the air. The reflection spectrum of the transparent glaze model can be obtained after calculating a series of outgoing light intensities with different wavelengths.

D. Estimation of model parameters

According to Fresnel formula, the reflection rate of incident natural light at the glaze-air interface is

$$r_1 = \frac{1}{2} \left\{ \left[-\frac{\sin(\theta_1 - \theta_2)}{\sin(\theta_1 + \theta_2)} \right]^2 + \left[\frac{\tan(\theta_1 - \theta_2)}{\tan(\theta_1 + \theta_2)} \right]^2 \right\},$$

where θ_1 and θ_2 are incident angle and refraction angle, respectively, and they satisfy refraction law $\sin \theta_1 = n_0 \sin \theta_2$, where n_0 is the refraction index and can be reduced into $r_1 = \left(\frac{n_0 - 1}{n_0 + 1} \right)^2$ under the normal incidence condition. The ancient copper red glaze is a typical high temperature calcium alkali glaze, and its refraction is around 1.5. In this work, we choose 1.52, and the corresponding reflection rate r_1 is about 0.04.

The whiteness of the white porcelain body in the Ding kiln can exceed 70%. As an estimation, the reflectivity r_2 of the body is taken as 0.7.

The absorption effect of transparent glaze is obviously related to the thickness and type of glaze. As an estimation, we assume that the light attenuates to 90% of the original intensity after passing through the transparent glaze without copper-containing particles, which is to say, s_0 is taken as 0.90.

In the computational simulation, the glaze thickness is set to 200 μm , which is the typical thickness of the red layer of copper red glaze observed in our previous experiment; the thickness t of each thin layer is 5 times the particle diameter, which can ensure that the interaction between particles is small and then meet the far-field conditions of Mie scattering as much as possible.

As for the properties of colorant nanoparticles, previous research studies have revealed that the nanoparticles in the copper red glaze can be circular or polygonal in shape, and their diameters mainly fall in the interval of 50–100 nm.^{1,3} Therefore, in our simulation, we choose the diameters to be 20, 50, 100, and 200 nm to fit previous experimental results.

It should be pointed out here that the numerical calculation framework given above has many similarities with the classical four-flux model^{21,22} in terms of physical ideas, and the four-flux model can give analytical solutions. However, the advantage of our model is that it can be easily extended to non-uniform systems, such as the common multilayer glaze of ancient ceramics, and the system

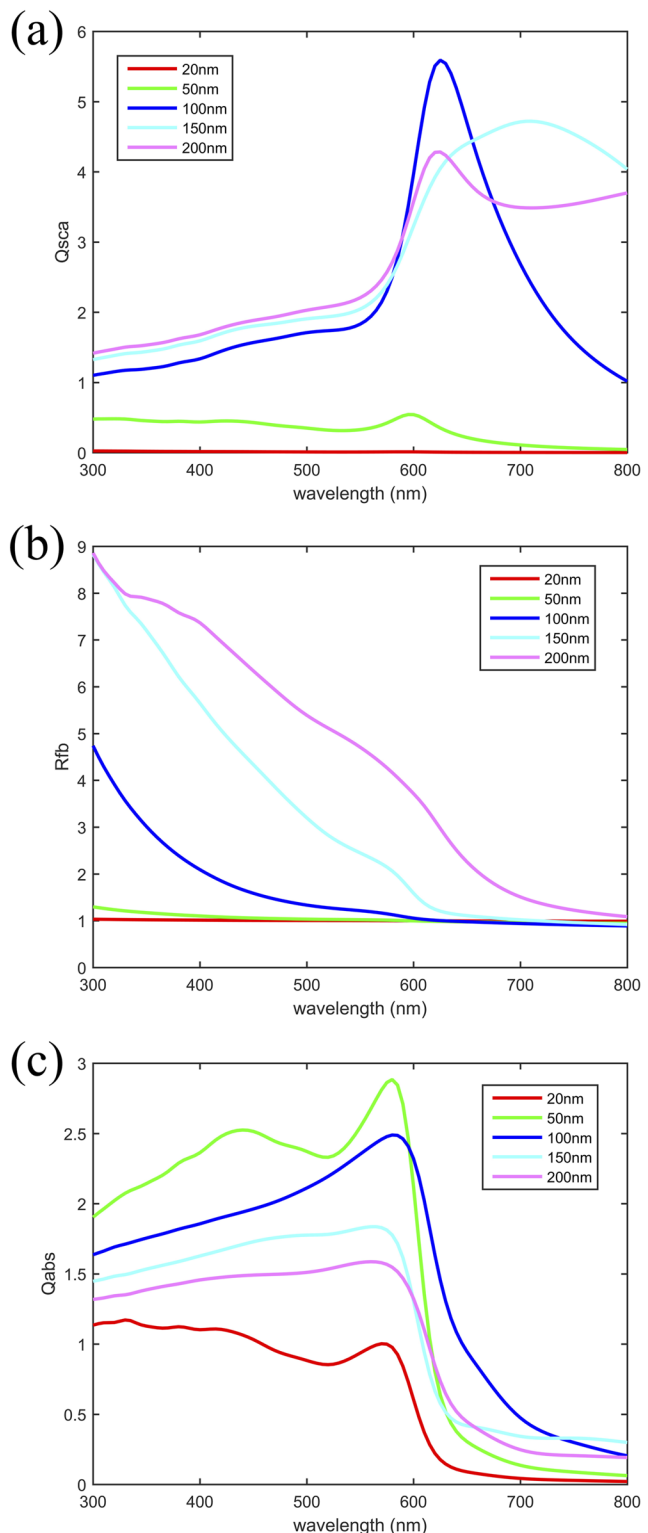


FIG. 3. (a) Scattering coefficient Q_{sca} , (b) forward/backward scattering rate R_{fb} , and (c) absorption coefficient Q_{abs} of metallic copper particles with different particle sizes for light with different wavelengths.

in which the particle size and number density of scattering particles change with depths in some middle-east areas.^{8,23}

E. CIE-L^{*}a^{*}b^{*} color space

In order to describe the color of a particular object, the best way is to measure its reflection spectrum, but it is really inconvenient. Considering the fact that there are three kinds of optic cone cells, which are sensitive to blue, green, and red colors, respectively, the so-called tristimulus values X , Y , and Z are introduced to describe the responses of these three kinds of cells to the reflected light,

$$\begin{cases} X = k \sum_{\lambda} R(\lambda) S(\lambda) \bar{x}(\lambda) \Delta \lambda, \\ Y = k \sum_{\lambda} R(\lambda) S(\lambda) \bar{y}(\lambda) \Delta \lambda, \\ Z = k \sum_{\lambda} R(\lambda) S(\lambda) \bar{z}(\lambda) \Delta \lambda, \end{cases}$$

where $R(\lambda)$ is the reflected intensity coefficient, $S(\lambda)$ is the relative spectral power distribution of standard light source, and $\bar{x}(\lambda)$,

$\bar{y}(\lambda)$, and $\bar{z}(\lambda)$ are color matching functions of standard colorimetric observer, and a set of (X , Y , Z) values corresponds to a certain color.

Based on tristimulus values X , Y , and Z , several different color spaces can be defined such as RGB, L^{*}c^{*}h^{*}, and L^{*}a^{*}b^{*}. The color space L^{*}a^{*}b^{*} used in this manuscript is defined as

$$\begin{cases} L^* = 116 f\left(\frac{Y}{Y_n}\right) - 16, \\ a^* = 500 \left(f\left(\frac{X}{X_n}\right) - f\left(\frac{Y}{Y_n}\right) \right), \\ b^* = 200 \left(f\left(\frac{Y}{Y_n}\right) - f\left(\frac{Z}{Z_n}\right) \right), \end{cases}$$

where

$$f(t) = \begin{cases} \sqrt[3]{t} & \text{if } t \leq \delta^3, \delta = \frac{6}{29} \\ \frac{t}{3\delta^2} + \frac{4}{29} & \text{if } t > \delta^3 \end{cases}$$

and $X_n = 95.0489$, $Y_n = 100$, and $Z_n = 108.8840$.

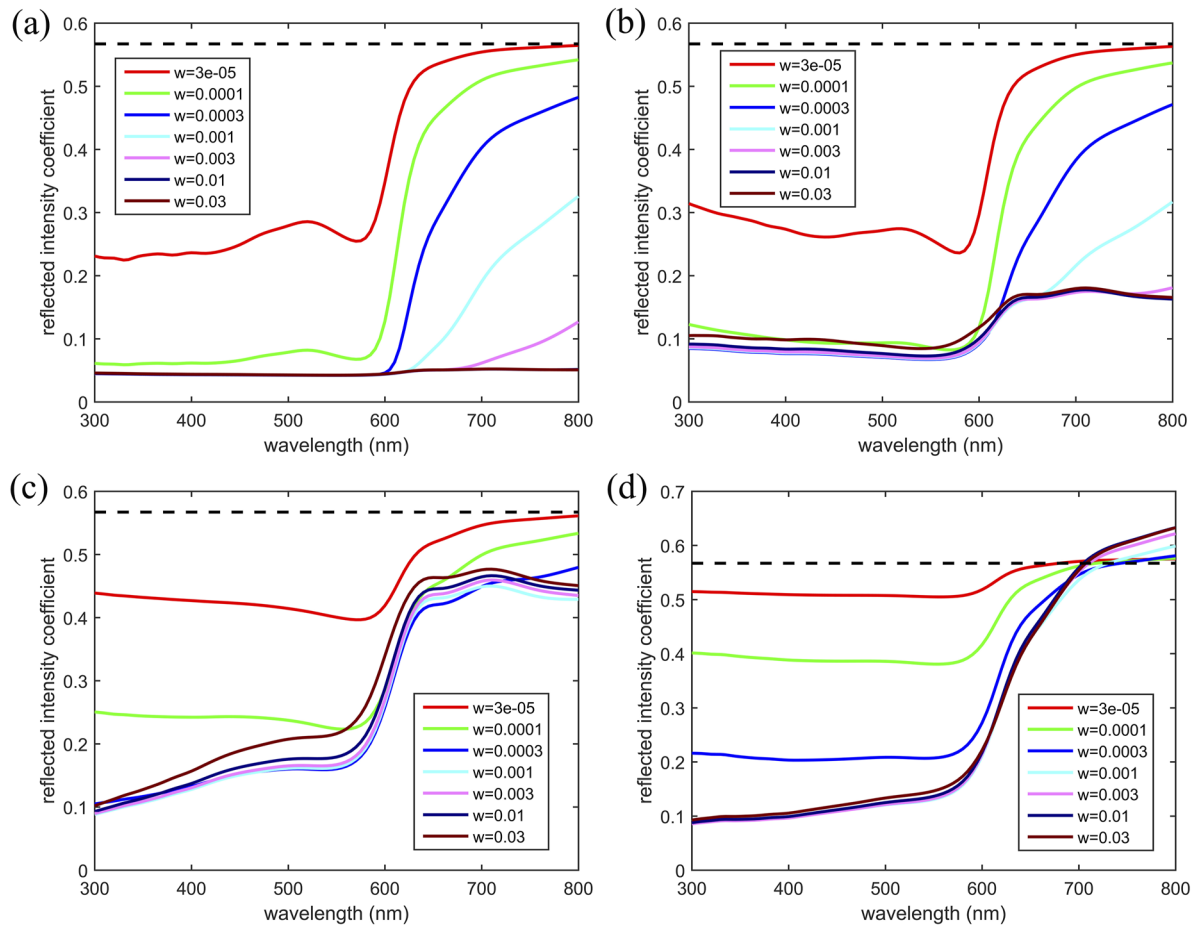


FIG. 4. Reflection spectra of metallic copper particles with diameters of (a) 20 nm, (b) 50 nm, (c) 100 nm, and (d) 200 nm under different volume fractions. The black dotted lines represent the reflection spectra of pure transparent glaze without any nanoparticles.

Contrary to (X, Y, Z) values, (L^*, a^*, b^*) values are more intuitive: L^* presents the brightness, and the object looks brighter when L^* is larger; a^* depicts the red-green hue, the object looks redder when a^* is larger, and greener when a^* is smaller; b^* depict the yellow-blue hue, the object looks yellower when b^* is larger, and bluer when b^* is smaller. L^* ranges from 0 to 100, and both a^* and b^* range from -128 to +127.

III. RESULTS AND DISCUSSION

A. Metallic copper particles as scatterers

Figure 3 shows the calculation results of scattering coefficient Q_{sca} , forward/backward scattering rate R_{fb} and absorption coefficient Q_{abs} of metallic copper particles with different particle sizes for different wavelengths of light. The optical constant data used are taken from the paper of Johnson and Christy.²⁴

It is not difficult to see that for copper particles with diameters in the range of 20–200 nm, the peak position of scattering coefficient Q_{sca} appears in the range of 600–700 nm, and the scattering coefficient of copper particles with a diameter of 100 nm for light with a wavelength near 620 nm is close to 6. The variation trend of absorption coefficient Q_{abs} of copper particles with different particle sizes for light with wavelength is roughly the same: for

the light with wavelength below 600 nm, the absorption coefficient is larger, while near 600 nm, the absorption coefficient decreases precipitously.

The forward/backward scattering rate R_{fb} of copper particles with different particle sizes is obviously different, but the variation trend is also obvious. Theoretically, when the particle size is much smaller than the wavelength of the incident light, the forward and backward scattering intensities are equal, which corresponds to the Rayleigh scattering. Therefore, for particles with diameters of 20 nm and 50 nm, the forward/backward scattering rate R_{fb} is basically equal to 1; for particles with a larger size, the forward/backward scattering rate R_{fb} first decreases rapidly with an increase in incident light wavelength and then oscillates near $R_{\text{fb}} = 1$. Therefore, for some specific wavelengths and particle sizes, the light scattered backward will have a higher intensity than the light scattered forward.

Based on the parameters above, we calculated the reflection spectra of metallic copper particles with particle sizes of 50, 100, and 200 nm under different volume fractions, as shown in Fig. 4. Generally speaking, its common feature is that the reflectivity is low in the range of 300–600 nm while increasing rapidly and stabilizing at another higher value after passing through an interval of less than 50 nm. Such a feature is also consistent with the measured reflection spectra of copper red glaze previously reported.^{13,25}

TABLE I. $L^* a^* b^*$ values of reflection spectra produced by metallic copper particles.

| Volume fraction | 0.00003 | 0.0001 | 0.0003 | 0.001 | 0.003 | 0.01 | 0.03 |
|--------------------|---------|--------|--------|-------|-------|------|------|
| 20 nm | L^* | 61.6 | 39.2 | 28.2 | 25.0 | 24.6 | 24.6 |
| | a^* | 11.1 | 27.0 | 19.7 | 3.9 | 1.5 | 1.5 |
| | b^* | 7.5 | 13.8 | 6.2 | 0.8 | 0.1 | 0.05 |
| Color ^a | | | | | | | |
| 50 nm | L^* | 60.2 | 40.3 | 34.6 | 33.9 | 34.2 | 35.0 |
| | a^* | 10.7 | 22.1 | 15.4 | 11.0 | 11.0 | 10.8 |
| | b^* | 3.0 | 6.2 | 3.0 | 1.6 | 1.5 | 1.4 |
| Color ^a | | | | | | | |
| 100 nm | L^* | 70.5 | 57.4 | 51.3 | 51.7 | 52.2 | 53.6 |
| | a^* | 4.1 | 12.0 | 17.4 | 17.7 | 17.7 | 17.2 |
| | b^* | -0.8 | 1.9 | 9.6 | 10.5 | 10.5 | 10.9 |
| Color ^a | | | | | | | |
| 200 nm | L^* | 76.8 | 69.3 | 55.6 | 47.0 | 47.3 | 47.8 |
| | a^* | 1.8 | 5.7 | 13.8 | 19.5 | 19.6 | 19.1 |
| | b^* | 0.3 | 1.4 | 5.6 | 13.1 | 13.6 | 13.5 |
| Color ^a | | | | | | | |

^aThe colors are recreated by <https://www.qtccolor.com/secaiku/tool/convert?m=lab>

Furthermore, with the help of colorimetry, we can calculate the corresponding $L^*a^*b^*$ values according to the simulated reflection spectrum, which can objectively and quantitatively characterize the color of objects. Generally speaking, the larger the a^* value is, the more obvious the red is. Table I presents the corresponding calculation results and recreated colors for each simulation condition. If $a^* > 15$ is taken as the criterion for a good coloration effect, it can be seen from Table I and Fig. 4 that when the diameter of copper particles is 50 nm, a good coloration effect can be achieved when the volume fraction is in the range of 0.003%–0.03%, and the effect becomes worse when the content is higher; when the diameter is 100 nm, good coloration effect can be achieved when the volume fraction exceeds 0.03%; when the particle size is 200 nm, the volume fraction of particles needs to be at least 0.1%.

B. Cuprous oxide (Cu_2O)

Figure 5 shows the calculation results of scattering coefficient Q_{sca} , forward/backward scattering rate R_{fb} , and absorption coefficient Q_{abs} of cuprous oxide particles with different particle sizes for different wavelengths of light. The optical constants used in the calculation are taken from the monograph edited by Palik.²⁶

Different from metallic copper particles, for Cu_2O particles, the peak position of scattering coefficient Q_{sca} moves from about 300 nm to about 600 nm with an increase in particle size from 50 to 200 nm, and the maximum value of scattering coefficient is about 3. The absorption coefficient Q_{abs} of Cu_2O particles with different diameters basically decreases with an increase in wavelength, and the change is relatively smooth, without precipitously decreasing as shown by copper particles at 600 nm. In addition, the change of forward/backward scattering rate R_{fb} of Cu_2O particles with different diameters is more complex. For example, for Cu_2O particles with diameters of 150 and 200 nm, there are two maxima and one minimum in the range of 300–800 nm.

On this basis, we further calculated the reflection spectra of cuprous oxide particles with diameters of 50, 100, and 200 nm under different volume fractions. As shown in Fig. 6, there is a significant difference between the reflection spectra generated by cuprous oxide and metallic copper particles. Although the reflection spectra also increase with an increase in wavelength, the intervals of the rising section are obviously wider than that of the corresponding reflection spectra of metallic copper particles, and their position gradually redshifts with an increase in particle size.

Table II presents the $L^*a^*b^*$ values and recreated colors of the system under different conditions when cuprous oxide particles are used as scatterers as well as recreated colors for each simulation condition. It is not difficult to find that except in the case that $d = 20 \text{ nm}$, $\omega = 0.3\%$, the a^* value of the corresponding reflection spectra in other cases is less than 15; that is to say, it is not red enough. What is more, the relationship $b^* > a^*$ is common in Table II, which means that when the scatterer is cuprous oxide, the system will intuitively appear as a mixed color of red and yellow rather than bright red.

C. Comparison with experimental results

As a comparison, we found the measured chromaticity value of sacrificial red glaze in the Ming and Qing Dynasties in the literature, as presented in Table III.

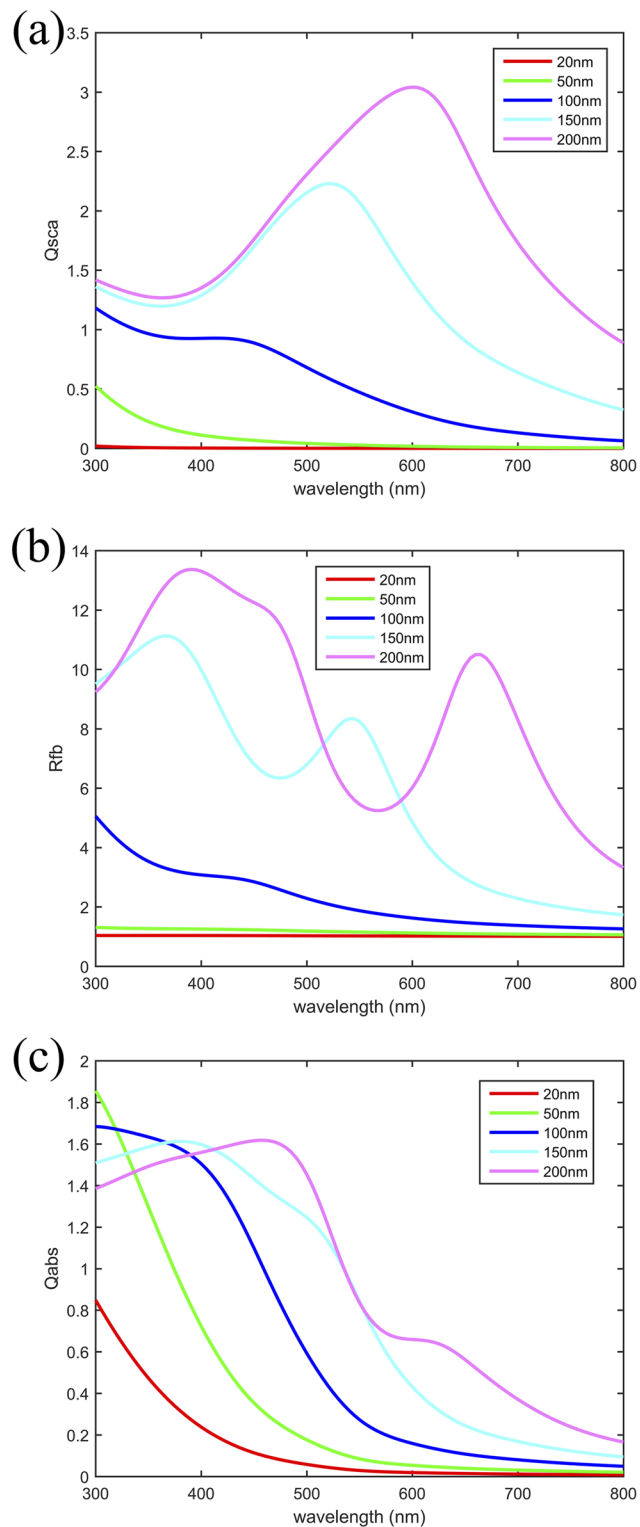


FIG. 5. (a) Scattering coefficient Q_{sca} , (b) forward/backward scattering rate R_{fb} , and (c) absorption coefficient Q_{abs} of cuprous oxide particles with different diameters for the light of different wavelengths.

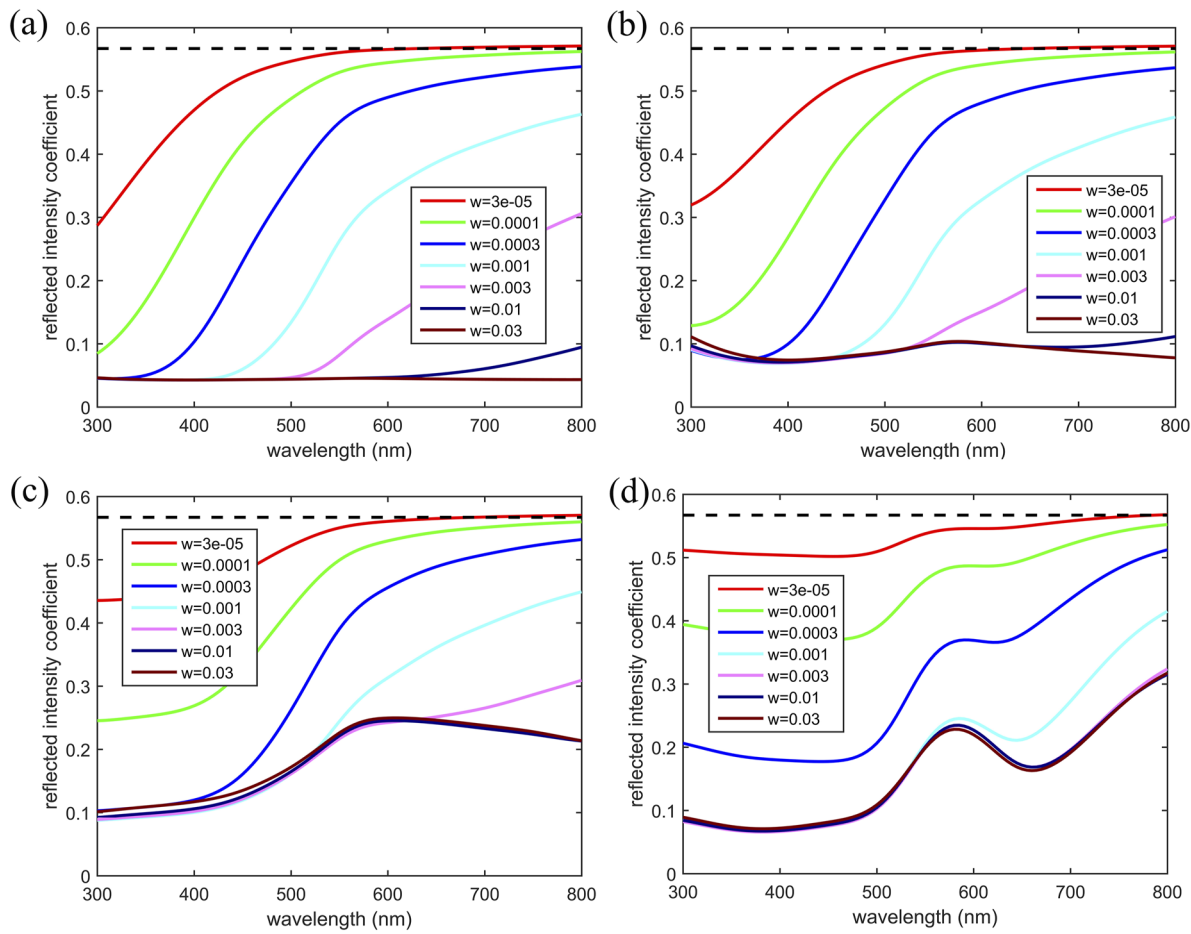


FIG. 6. Reflection spectra of cuprous oxide particles with diameters of (a) 20 nm, (b) 50 nm, (c) 100 nm, and (d) 200 nm under different volume fractions. The black dotted lines represent the reflection spectra of pure transparent glaze without any nanoparticles.

In order to facilitate understanding, the data in the above three tables can be drawn in the same figure. Considering that the values of a^* and b^* are more closely related to coloration, we choose b^* as the horizontal coordinate and a^* as the vertical coordinate to draw the scatter diagram, as shown in Fig. 7.

It is not difficult to see from Fig. 7 that when the scatterers are metallic copper particles, their a^* values basically fall on the left side of the blue dotted line $a^* = 3b^*/2$, and all of them fall on the left side of the cyan dotted line $a^* = b^*$, which is in sharp contrast to Cu_2O particles. Moreover, the measured chromaticity values of sacrificial red glaze samples also fall in the corresponding area of metallic copper particles, which further proves that sacrificial red glaze mainly depends on metallic copper particles as the colorant.

It should be noted that whether there are Cu_2O particles in the glaze cannot be determined just based on the results of the reflection spectrum. In previous literature, researchers judged the coloration mechanism simply by analyzing the phase of crystalline particles in glaze, which may not be reliable. According to the results of this

paper, it is difficult for cuprous oxide particles as scatterers in the transparent glaze to give bright red. Therefore, if the reflection spectrum of the sample shows the characteristics of typical copper red glaze, that is to say, it rises rapidly near 600 nm and the chromaticity value $a^* > 3b^*/2$, then it can be considered that its colorant is mainly the metallic copper particles, even if both metallic copper particles and cuprous oxide particles do exist in the system simultaneously. If the increasing interval of the reflection spectrum is wide and the chromaticity value $b^* > a^*$, a cuprous oxide is likely to play a role in coloration.

As an application, we analyzed one furnace transmutation copper red glaze sample shown in Fig. 8(a), which was produced during the Qianlong reign period in the Qing Dynasty and unearthed from the Nandaku site in the Palace Museum. Figure 8(b) shows the optical dark field image of the cross-section sample. It can be seen that the glaze can be divided into three layers: the top transparent layer, the red layer, and the bottom transparent layer.

Figure 8(c) shows three reflection spectra measured at three different points of the sample, which rise rapidly near 600 nm. The

TABLE II. L^* - a^* - b^* values of reflection spectra produced by cuprous oxide particles.

| Volume fraction | 0.000 03 | 0.0001 | 0.0003 | 0.001 | 0.003 | 0.01 | 0.03 | |
|-----------------|--------------------|--------|--------|-------|-------|------|------|--|
| 20 nm | L^* | 79.5 | 77.3 | 71.5 | 57.0 | 36.2 | 25.4 | |
| | a^* | -0.5 | -1.1 | -0.3 | 9.4 | 15.9 | 1.0 | |
| | b^* | 3.7 | 11.4 | 27.7 | 44.3 | 19.6 | 0.1 | |
| 50 nm | Color ^a | | | | | | | |
| | L^* | 79.3 | 76.8 | 70.5 | 56.0 | 40.8 | 37.0 | |
| | a^* | -0.6 | -1.2 | 0.5 | 10.9 | 9.2 | -0.2 | |
| 100 nm | b^* | 4.5 | 13.7 | 30.7 | 36.0 | 13.0 | 6.1 | |
| | Color ^a | | | | | | | |
| | L^* | 78.7 | 75.1 | 67.4 | 56.3 | 52.7 | 53.1 | |
| 200 nm | a^* | -0.3 | 0.1 | 4.5 | 9.0 | 2.7 | 2.1 | |
| | b^* | 6.3 | 18.1 | 32.9 | 25.1 | 18.4 | 18.1 | |
| | Color ^a | | | | | | | |
| 200 nm | L^* | 78.0 | 72.9 | 62.2 | 50.2 | 49.2 | 49.3 | |
| | a^* | 0.9 | 2.7 | 6.0 | 5.5 | 3.6 | 3.4 | |
| | b^* | 3.0 | 9.3 | 21.6 | 28.2 | 27.0 | 26.6 | |
| 200 nm | Color ^a | | | | | | | |

^aThe colors are recreate by <https://www.qtccolor.com/secaiku/tool/convert?m=lab>.

averaged chromaticity values calculated are $L^* = 33.0$, $a^* = 17.7$, and $b^* = 7.1$, which also satisfies the relation $a^* > 3b^*/2$. According to the theory discussed above, the colorant should mainly be the metallic copper particles.

TABLE III. Measured chromaticity values of sacrificial red glaze in Ming and Qing Dynasties.

| Dynasty | Sample number | L | a | b |
|-----------------------|-------------------|------|------|-----|
| Ming ²⁷ | YL-1-1 | 28.4 | 13.9 | 6.4 |
| | YL-1-2 | 26.5 | 20.1 | 8.2 |
| | YL-1-3 | 20.4 | 23.1 | 7.7 |
| | XD-1-1 | 26.2 | 20.2 | 7.7 |
| | XD-1-2 | 12.3 | 17.4 | 5.7 |
| | XD-1-3 | 22.5 | 24.9 | 7.8 |
| Qing ^{27,28} | KX-1 | 28.5 | 23.9 | 7.8 |
| | YZ-1 | 19.3 | 16.0 | 4.8 |
| | QL-1 | 27.5 | 16.4 | 5.7 |
| | QL-2 ^a | 14.7 | 11.7 | 4.0 |
| | DG-1 ^a | 22.8 | 12.9 | 4.5 |

^aThe colors of these two samples are pig liver-colored and dark red, which are not representative enough.

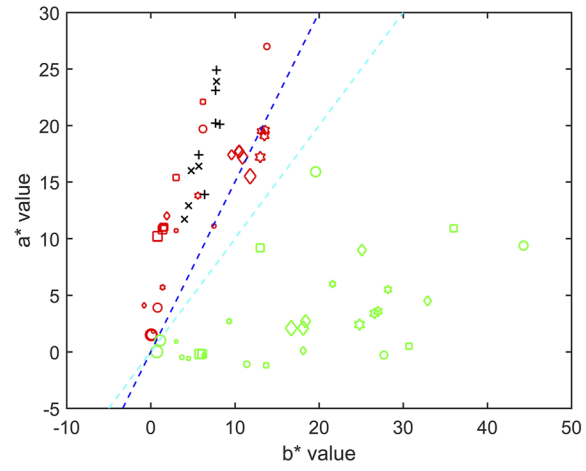
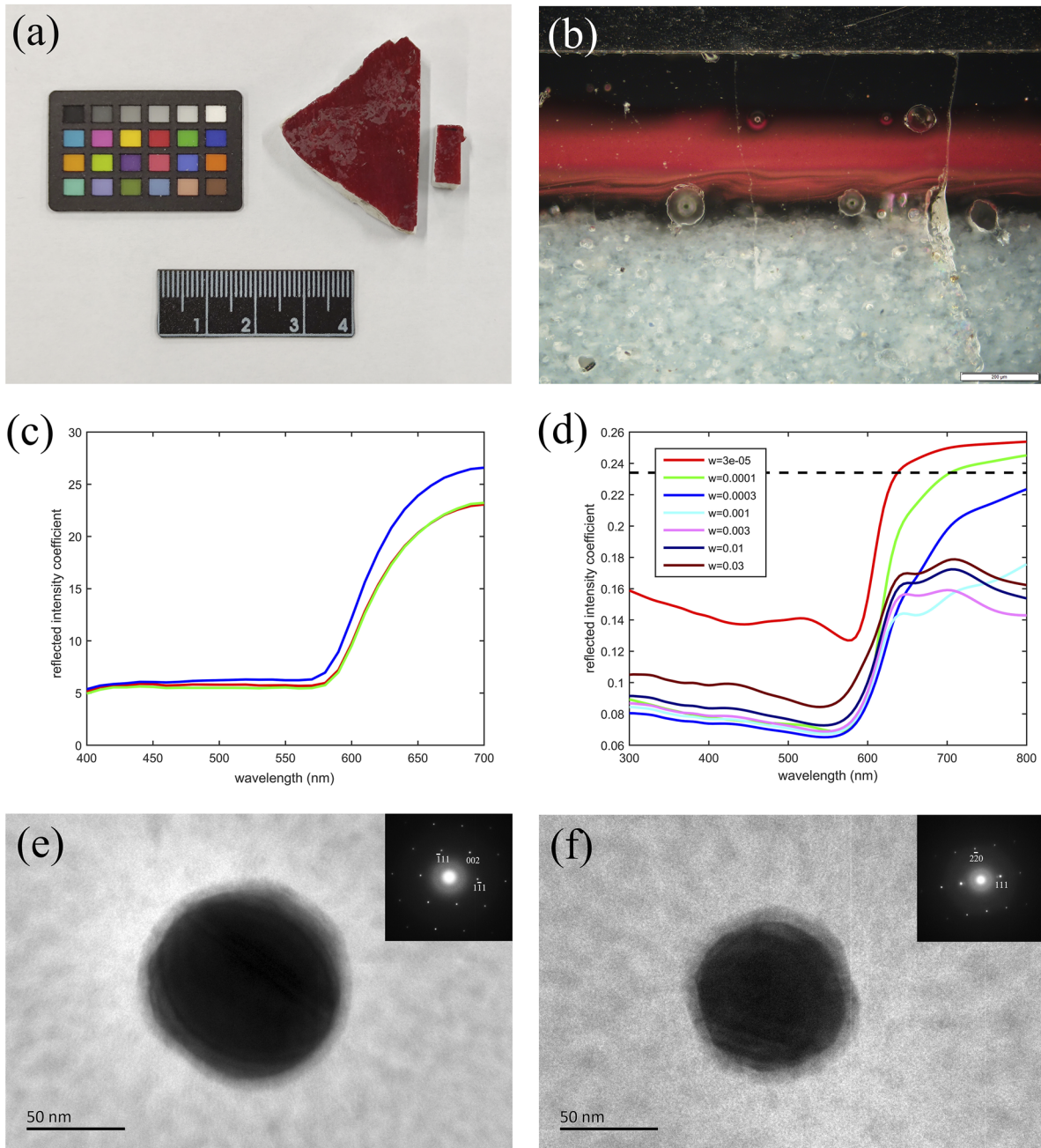


FIG. 7. Chromaticity a^* and b^* values corresponding to simulated reflection spectra and experimental results. The red and green colors represent the case where the scatterers are metallic copper and cuprous oxide particles, respectively; the round, square, diamond, and hexagonal shapes represent the diameters of 20, 50, 100, and 200, respectively, and the figures from small to large represent seven different volume fractions. In addition, the “+” in black represents the measured chromaticity value of the sacrificial red glaze of the Ming Dynasty, while the “x” in black represents the measured chromaticity value of the sacrificial red glaze of the Qing Dynasty. Blue dotted line is $a^* = 3b^*/2$, and cyan dotted line is $a^* = b^*$.



In fact, the reflection spectrum can also be simulated, as shown in Fig. 8(d), where the diameter of copper nanoparticles in simulation is 50 nm. However, the other parameters used here are a little different from previous simulations: the measured reflectivity of this ceramic body is about 65%, so the reflection rate r_2 is

chosen as 0.65; meanwhile, the absorption coefficient s_0 is decreased from 0.90 to 0.6 because the total thickness of glaze is much larger than that of the red layer. It can be seen that the simulated reflection spectrum with $w = 0.0001$ (green line) is quite similar to the experimental results, which indirectly prove that the colorant of this

sample may be metallic copper nanoparticles with a diameter of around 50 nm.

Direct evidence is given by TEM, as shown in Figs. 8(e) and 8(f), where the shapes of such nanoparticles are close to the sphere with diameters of 50–100 nm, and the diffraction patterns in the upper-right corner demonstrate that these nanoparticles are really pure metallic copper particles.

The reflection spectra were measured by colorimeter CHN Spec CS-520. The FIB cutting of the TEM sample was conducted with a Zeiss Auriga Compact dual beam instrument equipped with an Omniprobe AutoProbe 200 micromanipulator at IGGCAS (Institute of Geology and Geophysics, Chinese Academy of Science). Ion beam conditions for the final thinning and polishing were 5–30 kV high voltage with beam currents of 50 pA–2 nA. The FIB section was prepared to about 100 nm and $10 \times 3 \mu\text{m}^2$ in area. The TEM imaging and selected area electron diffraction were carried out using a JEOL JEM-2100 TEM operated at 200 kV with Oxford X-MAX energy dispersive x-ray spectrometers at IGGCAS.

IV. CONCLUSION

In this paper, using the computational simulation method based on multiple scattering and aiming at the situation that the copper-containing particles are uniformly distributed in the copper red glaze, the reflection spectra of the glaze with different particle sizes, different volume fractions, and different kinds of nanoparticles are calculated. The calculation results show that the metallic copper particles in the range of diameter from 20 to 200 nm may make the glaze appear as a good copper red glaze, but the volume fraction required changes as the size changes. When cuprous oxide nanoparticles are used as scatterers, their spectral characteristics are obviously different from that produced by metallic copper particles, so it is difficult to achieve the effect of the copper red glaze. The chromaticity value of the sacrificial red glaze reported in the literature is consistent with our calculation results for metallic copper particles, and our experiments with the copper red glaze sample also support our simulation results. In this sense, we can quickly judge the coloration mechanism by analyzing its reflection spectrum.

ACKNOWLEDGMENTS

The authors would like to thank Jiayu Hou, An Gu, Yao Chen, and Dr. Ming Guan for their help with this work. We thank Xu Tang and Lixin Gu at the Electron Microscopy Laboratory, Institute of Geology and Geophysics, Chinese Academy of Science, for their efforts to maintain smooth operation in FIB-SEM and TEM experiments. This work was financially supported by the Chinese National Natural Science Foundation (Grant Nos. U1832164 and U1932203).

AUTHOR DECLARATIONS

Conflict of Interest

The authors have no conflicts to disclose.

Author Contributions

Gen Li: Conceptualization (equal); Data curation (lead); Methodology (lead); Software (lead); Writing – original draft (lead); Writing – review & editing (equal). **Yong Lei:** Conceptualization (equal); Funding acquisition (lead); Resources (lead).

DATA AVAILABILITY

The data that support the findings of this study are available from the corresponding author upon reasonable request.

REFERENCES

- ¹C. Jia, G. Li, M. Guan, J. Zhao, Y. Zheng, G. Wang, X. Wei, and Y. Lei, *J. Eur. Ceram. Soc.* **41**(6), 3809–3815 (2021).
- ²S. Tian, Y. Liu, M. Zhang, L. Wang, Y. Xie, and C. Wang, *Nucl. Tech.* **32**(06), 413–418 (2009).
- ³J. Hou, C. Jia, X. Zhang, H. Li, G. Li, H. Liu, B. Kang, and Y. Lei, *J. Eur. Ceram. Soc.* **42**(3), 1141–1148 (2022).
- ⁴Y. Luo, W. Pan, S. Li, H. Zhao, and J. Wang, *Ceramics* **2000**(06), 23–26 (2000).
- ⁵M. Wakamatsu, N. Takeuchi, H. Nagai, Y. Ono, and S. Ishida, *J. Ceram. Soc. Jpn.* **94**(4), 387–392 (1986).
- ⁶J. Hou, T. Pradell, Y. Li, and J. Miao, *J. Eur. Ceram. Soc.* **38**(12), 4290–4302 (2018).
- ⁷T. Pradell, G. Molina, J. Molera, J. Pla, and A. Labrador, *Appl. Phys. A* **111**, 121–127 (2013).
- ⁸G. Molina, M. S. Tite, J. Molera, A. Climent-Font, and T. Pradell, *J. Eur. Ceram. Soc.* **34**(10), 2563–2574 (2014).
- ⁹Y. Wang, S. Yu, M. Tong, W. Wang, and X. Yang, *J. Cult. Heritage* **48**, 29–35 (2021).
- ¹⁰J. Xue, J. Zhong, Y. Mao, C. Xu, W. Liu, and Y. Huang, *Ceram. Int.* **46**(14), 23186–23193 (2020).
- ¹¹M.-L. Zhang, L.-H. Wang, L.-L. Zhang, and H.-S. Yu, *Nucl. Sci. Tech.* **30**, 114 (2019).
- ¹²G. Chen, S. Chu, T. Sun, X. Sun, L. Zheng, P. An, J. Zhu, S. Wu, Y. Du, and J. Zhang, *J. Synchrotron Radiat.* **24**, 1000 (2017).
- ¹³C. Lu, J. Jiang, C. Xu, S. Wu, L. Guan, J. Zhang, D. Chen, W. Xu, J. Zhuand, and C. Wang, *J. Univ. Chin. Acad. Sci.* **33**(03), 421–426 (2016).
- ¹⁴Y. Li, Y. Yang, J. Zhu, X. Zhang, S. Jiang, Z. Zhang, Z. Yao, and G. Solbrekken, *Ceram. Int.* **42**(7), 8495–8500 (2016).
- ¹⁵J. Zhu, H. Duan, Y. Yang, L. Guan, W. Xu, D. Chen, J. Zhang, L. Wang, Y. Huang, and C. Wang, *J. Synchrotron Radiat.* **21**, 751–755 (2014).
- ¹⁶I. Nakai, C. Numako, H. Hosono, and K. Yamasaki, *J. Am. Ceram. Soc.* **82**(3), 689–695 (1999).
- ¹⁷T. Pradell, R. S. Pavlov, P. C. Gutiérrez, A. Climent-Font, and J. Molera, *J. Appl. Phys.* **112**, 054307 (2012).
- ¹⁸P. A. Cuvelier, C. Andraud, D. Chaudanson, J. Lafait, and S. Nitsche, *Appl. Phys. A* **106**, 915–929 (2011).
- ¹⁹C. F. Bohren and D. R. Huffman, *Absorption and Scattering of Light by Small Particles*. John Wiley & Sons (1983).
- ²⁰C. Mätzler, MATLAB Functions for Mie Scattering and Absorption, 2002.
- ²¹B. Maheu, J. N. Letoulouzant, and G. Gouesbet, *Appl. Opt.* **23**(19), 3353–3362 (1984).
- ²²B. Maheu and G. Gouesbet, *Appl. Opt.* **25**(7), 1122–1128 (1986).
- ²³P. Sciau, L. Noé, and P. Colombar, *Ceram. Int.* **42**(14), 15349–15357 (2016).
- ²⁴P. B. Johnson and R. W. Christy, *Phys. Rev. B* **6**(12), 4370–4379 (1972).
- ²⁵C. Cao, H. Shen, J. Cao, C. Xiong, and N. Zheng, *China Ceram. Ind.* **9**(6), 4–8 (2002).
- ²⁶E. D. Palik, *Handbook of Optical Constants of Solids II* (Academic Press, 1998).
- ²⁷Q. Yu, Technology Study of the Qing Dynasty Sacrificial Red Glaze, 2013.
- ²⁸J. Wu, Q. Yu, M. Zhang, J. Wu, Q. Li, and Y. Wu, *J. Ceram.* **34**(04), 476–481 (2013).